Enhanced Perovskite Solar Cell Performance Via 2-amino-5-iodobenzoic Acid Passivation

*Jian Xiong, Pabitra Narayan Samanta, Yifang Qi, Teresa Demeritte, Kira Williams, Jerzy Leszczynski, and Qilin Dai**

Department of Chemistry, Physics and Atmospheric Sciences, Jackson State University, Jackson, MS, 39217, USA

KEYWORDS: inverted perovskite solar cells; 2-amino-5-iodobenzoic acid; passivation; efficiency; stability.

* Corresponding author: Q. Dai, Email: *qilin.dai@jsums.edu*

ABSTRACT

The intrinsic stability issues of the perovskite materials threaten the efficiency and stability of the devices, and the stability has become the main obstacle to industrial applications. Herein, the efficient and facile passivation strategy by 2-amino-5-iodobenzoic acid (AIBA) is proposed. The impact of AIBA on the properties of the perovskite films and device performance are systemically studied. The results show that the trap states are eliminated without affecting the crystal properties of the perovskite grains, leading to the enhanced performance and stability of the perovskite solar cells (PSCs). The high power conversion efficiency (PCE) of 20.23 % and lower hysteresis index (HI) of 1.49 ‰ are achieved, which represent one of the excellent PCE and HI values for the inverted PSCs based on $MAPbI_3$/PCBM planar heterojunction structure. Moreover, the UV stability of the perovskite films, thermal and moisture stability of the

devices are also enhanced by the AIBA passivation. The PCE of the device with AIBA can maintain about 83.41 % for 600 h (40 RH %), 64.06 % for 100 h (55-70 RH%) of its initial PCE value without any encapsulation, while the control device can only maintain about 72.91 % and 45.59 % of its initial PCE. DFT calculations are performed to study the origins of enhanced performance. Interestingly, the results show that the surface states induced by AIBA can facilitate the photoexcited charge transfer dynamics and reduce the electron-hole recombination loss. The passivation method developed in this work provides an efficient way to enhance the stability and performance of inverted PSCs.

INTRODUCTION

The perovskite solar cells (PSCs) based on organo-metal halide perovskite materials have attracted great attention because of their high photoelectric conversion efficiency, low cost, low-temperature process, and tunable bandgap [1-3]. Up to now, the highest recorded PCE of 25.5 % based on single-junction has been achieved [2]. This is comparable to many conventional inorganic photovoltaic devices and has great potential in large-scale production [4]. PSCs can be classified as regular (n-i-p) and inverted (p-i-n) structures depending on the type of charge transport material used in the transparent electrode side [5]. The inverted PSCs have the advantages of low abnormal hysteresis and low-temperature process [6]. Moreover, inverted PSCs also show more merits than regular PSCs in the preparation of high specific weight flexible PSCs [7] and wearable devices [8, 9]. However, the performance of inverted PSCs is unsatisfactory compared to regular PSCs (22.3 % for inverted PSCs vs 25.2 % for regular PSCs, according to certified records) [2, 10]. In addition, stability has always been the main barrier that hinders the application of PSCs due to the intrinsic stability issues of organo-metal halide perovskite materials [11]. Thus, many efforts are focused on the improvement of the performance and stability of inverted PSC [1, 10, 12-14].

The surface defects are inevitable in the polycrystalline perovskite films that are prepared at low temperatures via solution-based methods. This results in several orders of magnitude higher density of traps than in single crystals [15]. The defects cause non-radiative charge recombination loss [10]. Enlarging grain size is an efficient way to reduce the surface defects of the perovskite films [1, 12, 16, 17]. Perovskite grains with the size of

several micrometers are achieved via the nonwetting substrate, solvent annealing [12], or post-treatment [17]. However, the grain boundaries (GBs) cannot be completely removed, and the residual GBs represent vulnerable spots to trigger the degradation of the perovskite materials and the device performance [18, 19]. Recently, the strong surface recombination in single-crystalline $MAPbI_3$ without any GBs that resulted from higher surface trap densities has also been confirmed by a direct optical study [20]. Thus, efficient passivation strategies to passivate GBs and the surface trap states are necessary for preparing high-performance PSCs.

Many studies confirmed that the unsaturated or under-coordinated Pb ions may exist at the surface and GBs of polycrystalline perovskite films [21]. Furthermore, the theoretical modeling and experiment showed the under-coordinated Pb atoms are one of the main surface traps to limit the performance of the PSCs [15, 22]. Some Lewis bases , such as n-trioctylphosphine oxide [23], non-fullerenes [24, 25], urea [26], caprolactam [27] can donate electrons or share their electron pairs with un-coordinated Pb atoms and thus passivate this trap states. In addition, other kinds of defects also exist in solution-processed perovskite films, such as organoammonium vacancies, Pb interstitials, or I interstitials [28]. Although many efforts have been carried out based on passivation strategies to eliminate these defects, the elimination of surface defects is still a challenge due to the complexity and diversity of the surface defects [15, 26, 29-33]. Many organic passivation materials have been introduced into perovskite solar cells and some important results have been achieved [34]. The functional groups of the organic materials are also important to the passivation effect. Usually, the same functional groups in

different materials lead to different passivation effects in the perovskite layer [35-37]. Thus, the molecular structure also greatly influences the passivation effect. Secondly, many amino acid ligands affect the crystallization behavior of perovskite crystal growth [34, 38, 39] because the passivation materials were introduced in the process of perovskite growth. This influences the evaluation of the passivation effect of the material on the device performance due to the affected perovskite growth. Thirdly, the passivation of perovskite by post-treatment in regular PSCs is relatively easy because this structure is more tolerant to perovskite roughness [40, 41], while it is difficult for inverted PSCs by post-treatment. The inverted PSCs have high demanding requirements for the quality of the perovskite films [42].

In this work, we choose the 2-amino-5-iodobenzoic acid (AIBA) as the passivation material. Compared to other surface treatment or passivation strategies, there are some advantages. First, the benzene ring structure facilitates charge transportation and enhance the hydrophobicity of perovskite films [43]. Second, it doesn't influence the surface morphology and doesn't influence the crystallization behavior of polycrystalline perovskite films, which benefits understanding the surface passivation effects. Third, this material has strong UV light absorption, which benefits the UV light stability of the devices. Fourth, this material can passivate GBs as well as film surface defects, which can prevent moisture diffusion and ion migration, and thus enhance the moisture and interface stability. Finally, the AIBA exhibits some energy states near the conduction band edge of the perovskite, which facilitates the photoexcited charge transfer dynamics according to the calculation resutls. The AIBA introduced into

inverted PSCs via post surface treatment and the high power conversion efficiency (PCE) of 20.23 % and lower hysteresis index (HI) of 1.49 ‰ are achieved. This indicates excellent PCE and HI for inverted PSCs based on $MAPbI_3$ as the active layer. Moreover, the UV light stability of the perovskite films, thermal stability, and moisture stability of the devices are enhanced. The facile passivation strategy developed in this work provides an efficient way to passivate GB and surface defects due to the functional groups of the AIBA to enhance the stability and performance of inverted PSCs.

EXPERIMENT

Materials. Lead (II) iodide (PbI_2, 98 %), bathocuproine (BCP, >98 %) were purchased from TCI America. Poly[bis(4-phenyl) (2,4,6-trimethylphenyl) amine] (PTAA, >99 %), was obtained from Solaris Chem. (Canada). Methylammonium iodide (MAI, 99.5 %) was purchased from Xi'an Polymer Light Technology Corp. (China). PCBM (> 99 %), N,N-dimethylformamide (Super dry, DMF), AIBA (97 %), chlorobenzene (anhydrous, CB), and isopropyl alcohol (anhydrous, IPA) were obtained from Sigma-Aldrich (USA). Dimethyl sulfoxide (DMSO) and Ag wires (99.9 %) were purchased from Alfa Aesar (USA).

Device fabrication. In this work, the PSCs with the inverted structure (Figure 1a) were prepared according to our previous work [44]. For the preparation of the inverted PSCs, patterned ITO substrates were cleaned sequentially in soap, acetone, deionized water, and IPA for 15 min by an ultrasonic bath, respectively. Then, ITO substrates (~7 Ω/□) were treated by UV-ozone for 30 min. After that, the substrates were transferred into a glove box filled with N_2 (H_2O <1 ppm and O_2 < 1ppm), and the PTAA solution (3

mg/mL in toluene) was spin-coated onto ITO substrates at 4000 rpm for 30 s. Then the substrates were annealed at 100 ℃ for 10 min. The $MAPbI_3$ films were prepared by a two-step strategy. 1.2 M PbI_2 and 0.3 M MAI in DMF:DMSO (10:1) mix-solvent were prepared, and spin-coated upon PTAA at 6000 rpm for 20 s (step I) and 4000 rpm for 40 s (step II). During step II, the MAI solution (30 mg/mL in IPA) was dropped onto the center of the substrates. Finally, the substrates were annealed at 100 ℃ for 30 min to form the $MAPbI_3$ films. For the AIBA passivated films, the AIBA solution (0-3 mg/mL in IPA) was spin-coated on the top of $MAPbI_3$ films at 4000 rpm for 30 s and annealed at 70 ℃ for 10 min. After that, $PC_{61}BM$ (20 mg/mL in CB) was spin-coated on the top of the AIBA layer at 2000 rpm for 30 s and thermal annealing at 90 °C for 30 min. Finally, BCP solution (0.5 mg/mL in IPA) was spin-coated at 4000 rpm for 30 s, and then Ag cathodes (~100 nm) were fabricated via thermal evaporation under a vacuum of 6×10^{-4} Pa. The active area for all solar cells was 0.04 cm^2 defined by the shadow mask.

Characterizations. The micromorphology of films was measured by scanning electron microscopy (SEM) (Tescan, LYR3 XMH, USA). The crystallinity of the perovskite films was examined using an X-ray diffraction system (XRD) (Rigaku, MiniFlex 600, Japan). UV-vis absorption spectra were collected using a UV-vis spectrophotometer (Cary 60, Agilent, USA). The interation between AIBA and perovskite was characterized by an infrared spectrometer (PerkinElmer, Spectrum Two FT-IR, USA). The capacitance-voltage (C-V) curves were obtained using an electrochemical workstation (CHI, 604E, China) with a disturbance pulse bias voltage of 50 mV with

1K Hz. The electrochemical impedance spectroscopy (EIS) data of the devices were measured by applying 5 mV AC voltage whose frequency was swept from 1 Hz to 1M Hz in the dark. The current-voltage characteristics were measured using a Keithley 2400 sourcemeter (Keithley Instruments Inc.) under AM 1.5G simulated sunlight (100 mW cm^{-2}) (G2V, Pico solar simulator, Canada). The light intensity was calibrated using a Si solar cell (91150V, Newport). The incident photon-to-current efficiency (IPCE) spectra were measured by the quantum efficiency measurement system (Newport, IQE-200B, USA). The time-resolved PL spectra (TRPL) of films were measured by a fluorescence spectrophotometer (FluoroMax, Horiba) with TCSPC accessories under 460 nm light excitation. For the UV stability test, the UV lamp (6 Watt, 365 nm) was used to illuminate the perovskite films. In order to create a specific humidity environment to test the moisture resistance of the device, the environmental chamber (Electro-tech systems, 503, USA) was used to control the relative humidity of the environment of the devices. The details of density functional theory (DFT) calculations is provided in the supporting information.

RESULTS AND DISCUSSION

The small organic molecular structure of AIBA is shown in the inset of Figure 1a. The post-annealing process of the AIBA on perovskite films may promote the AIBA molecules diffusion into GBs and passivate the trap states of the top surface and GBs. The AIBA is selected as a passivant due to its unique structure. It has been reported that the -COOH and -I function groups can strongly coordinate with the positively charged un-coordinated Pb atoms [28, 29]. The group of $–NH_2$ may passivate the negatively charged

organoammonium vacancies or I interstitials (Figure 1b) [28, 29].

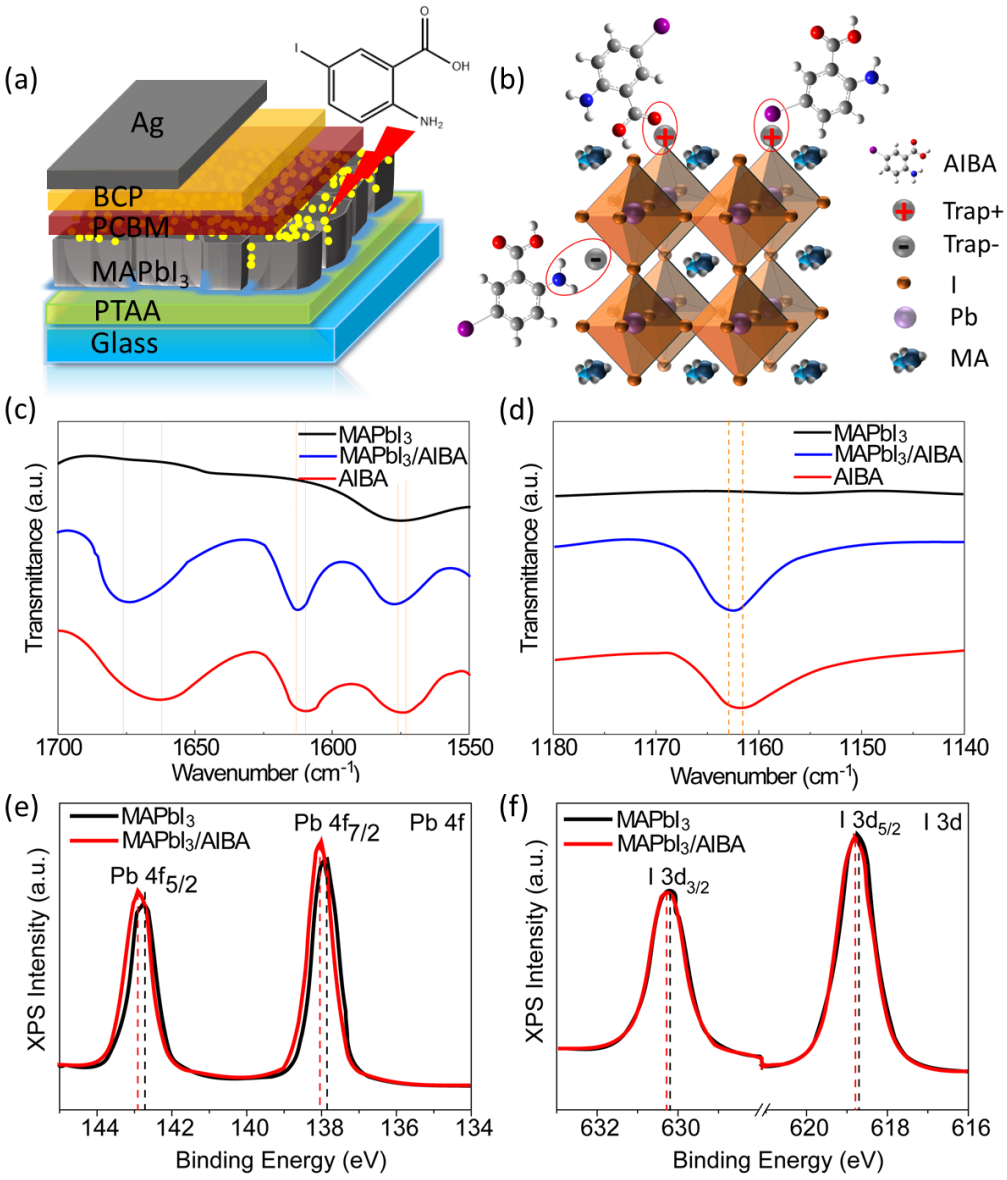

Figure 1. (a) Device structure of inverted PSCs. (b) Schematic of the interaction between AIBA molecules and $MAPbI_3$. (c) and (d) FTIR spectra of the $MAPbI_3$, AIBA and $MAPbI_3$/AIBA powder samples. (e) XPS spectra of the Pb 4f orbital of the $MAPbI_3$ film and $MAPbI_3$/AIBA film. (f) XPS spectra of the I 3d orbital of the $MAPbI_3$ film and $MAPbI_3$/AIBA film.

In order to prove the strong coordination between AIBA and $MAPbI_3$, the FTIR spectra of the $MAPbI_3$, AIBA, and $MAPbI_3$/AIBA powder samples are measured. The $MAPbI_3$ and $MAPbI_3$/AIBA powder samples are obtained by scrapping from the ITO substrates. The results are shown in Figure 1c and Figure 1d. For the AIBA sample, the symmetric stretching vibration of the C=O (ν(C=O)) is located at 1662 cm^{-1} [45] and the stretching vibrations of the C=C ring (νC=C ring)) is located at 1609 cm^{-1} [46] (Figure 1c). These characteristic peaks are also present in $MAPbI_3$/AIBA sample, while the peak positions are shifts to 1675 cm^{-1} and 1613 cm^{-1} (Figure 1c). The FTIR peak of amine groups on AIBA at 1573 cm^{-1} shifts to 1578 cm^{-1} after coating upon $MAPbI_3$ (Figure 1b). In addition, the asymmetric C–O–C stretch is located at 1162 cm^{-1} [47] in AIBA, while this peak shifts to 1163 cm^{-1} in the $MAPbI_3$/AIBA film (Figure 1d). This shift confirms the strong coordination between AIBA and $MAPbI_3$ [11, 47, 48]. The XPS spectra of the perovskite films were collected and the results are shown in Figure 1. The XPS spectra of the high-resolution spectra of Pb ($4f_{5/2}$, $4f_{7/2}$) and I ($3d_{3/2}$, $3d_{5/2}$) are shown in Figure 1 e and f. In comparison to pristine $MAPbI_3$ film, the peaks of Pb 4f and I 3d of $MAPbI_3$/AIBA are shifted toward higher binding energies. The peak shift shows that the electron cloud density of Pb and I atoms have been influenced by AIBA introduction, which confirms the strong interactions between AIBA and $MAPbI_3$, and the uncoordinated ionic defects can be passivated by AIBA[49].

To unveil the binding nature of $MAPbI_3$/AIBA film, we place further emphasis on quantitative analysis of surface-molecule interactions by performing density functional theory (DFT) calculations on the PbI_2-rich $MAPbI_3$ (001) surface after the imposition

of AIBA moiety. Figures 2a portrays the fully relaxed geometry of the $MAPbI_3$ (001) slab with PbI_2-rich termination (left) and the $MAPbI_3$/AIBA composite (right), respectively. The surface-molecule interaction transpires through the aryl -CH and -NH_2 groups of the AIBA moiety, and the lowest energy structure on the potential energy hypersurface corresponds to that geometry in which AIBA is aligned in T-shape orientation on the perovskite surface. The equilibrium distance between two entities in the optimized structure of the composite is calculated to be 3.07 Å. Furthermore, the binding energy after administration of AIBA molecule on the (001) slab of PbI_2-rich $MAPbI_3$ is estimated to be 1.07 eV at the PBE/DZP level of theory, which is fairly significant compared to the interaction energy between the cyano-based π-conjugated molecules comprising indacenodithienothiophene and the PbI_2-rich $MAPbI_3$ as reported in an earlier study [50]. This suggests AIBA can stabilize the PbI_2-rich surface of perovskite.

Next, we have analyzed the spin-resolved projected density of states (PDOS) spectra of the slab model of $MAPbI_3$ and the $MAPbI_3$/AIBA composite without defects existing. Figure 2b displays the total DOS of the PbI_2-rich $MAPbI_3$ (001) surface together with the contribution of atomic orbitals of I and Pb projected onto the surface atoms of the perovskite. The valence band maximum (VBM) of the $MAPbI_3$ is mainly contributed by the I 5p orbitals, while the conduction band minimum (CBM) is chiefly composed of Pb 6p orbitals. The calculated total DOS spectra for the pristine and passivated surfaces are further compared in Figure 2c. It is evident that HOMO electron distributions of both the perovskite surfaces resemble each other, while the LUMO level

is perturbed due to the introduction of AIBA on the $MAPbI_3$ surface. To explore the impact of surface passivation on the band-edge states, the PDOS spectra of the

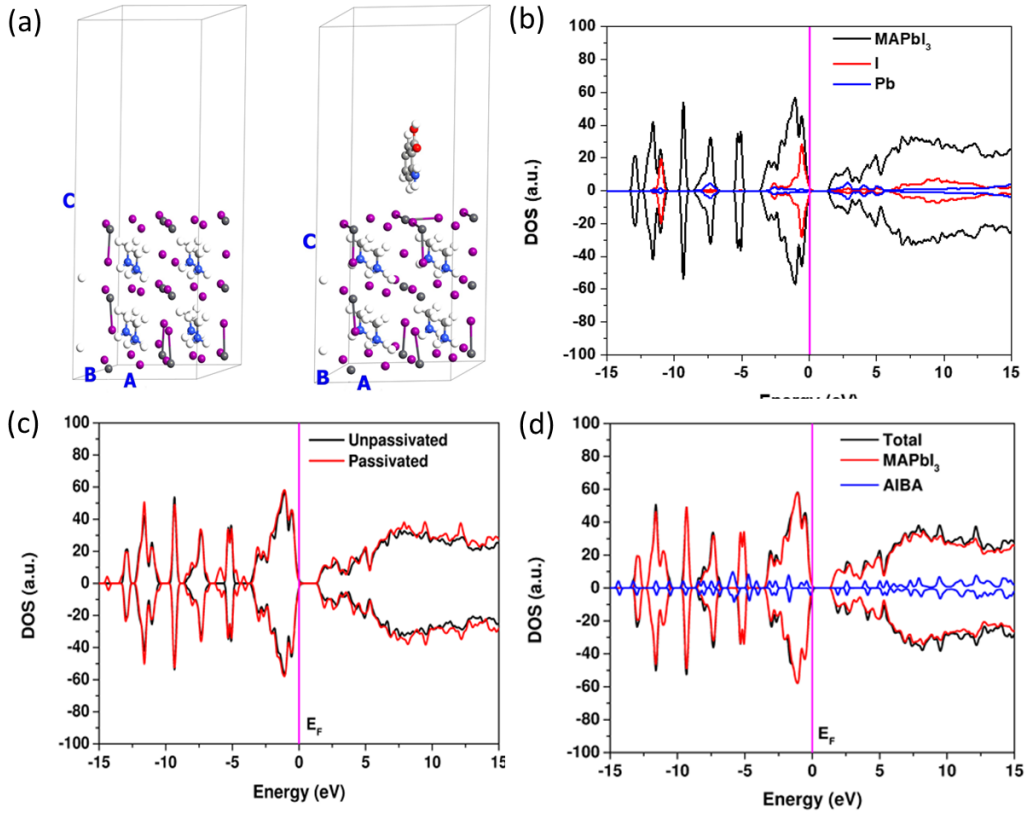

Figure 2. (a) Optimized geometry of (left) $MAPbI_3$ (001) slab with PbI_2-rich termination, and (right) $MAPbI_3$/AIBA composite. (b) Spin-resolved total density of states and projected density of states of Pb and I atoms in $MAPbI_3$ surface with PbI_2-rich termination. (c) Spin-resolved total density of states of $MAPbI_3$ with and without surface passivation. (d) Spin-resolved total density of states together with the projected density of states of $MAPbI_3$ and AIBA in the composite.

composite material are subsequently separated into the components stemming from the $MAPbI_3$ surface and the AIBA molecule, as shown in Figure 2d. The PDOS of AIBA

clearly demonstrates that the surface state produced by AIBA passivation on the $MAPbI_3$ with PbI_2-termination does not give rise to a deep electron trap. Furthermore, the AIBA has states near the CB edge of the perovskite, which in turn facilitate the photoexcited charge transfer dynamics without restraining the electron transfer process either to an electrode or to a photochemical reaction site. The electron-hole recombination rate is likely to be reduced by these surface states as they disintegrate from the hole. Thus, we estimate that the AIBA besides passivations has also positive effects for the charge transport.

Since the nonradiative recombination loss is one of the deleterious effects in limiting the PSC's performance caused by the charge carrier trapping at surface defects, we parallelly focus on quantitative analysis of defect formation on the PbI_2-rich $MAPbI_3$ (001) surface and their impact on the electrochemical performance of the perovskite material after surface passivation. Hybrid DFT calculations were carried out to estimate the defect formation energies due to the I atom vacancies (V_I), and MA vacancies (V_{MA}) on the PbI_2-rich $MAPbI_3$ surface, which may result in uncoordination Pb defects. Since the point defects in the organometal halide perovskites can be present in different oxidation states, the formation energies are evaluated for the neutral, cation, and anion vacancies at surface sites of the perovskite material. Among the three iodine vacancies, the defect formation energy of $MAPbI_3$ surface with V_I^- (-2.62 eV) is considerably lower than the V_I(2.95 eV) and V_I^+(8.69 eV). The formation of PbI_2-rich $MAPbI_3$ (001) surface with V_{MA}^+ is less favorable as substantiated by the computed defect formation energies for V_{MA}^+(13.70 eV) and V_{MA}^-(-2.48 eV). Next, we concentrate

on the estimation of formation energy after surface passivation by the AIBA molecule on the three lowest-energy defected perovskite surfaces comprising V_I^-, and V_{MA}^-. After the introduction of AIBA, the formation energy of V_I^-(2.95 eV) and V_{MA}^-(3.99 eV) is enhanced compared with the pristine $MAPbI_3$. The calculated closest distance between the AIBA and the defected surface sites is found to be 3.05 Å, and 2.89 Å, respectively, for the V_I^-, and V_{MA}^-. The calculated results show that AIBA can enhance the negatively charged defects formation energy, which suppresses the corresponding defects [50].

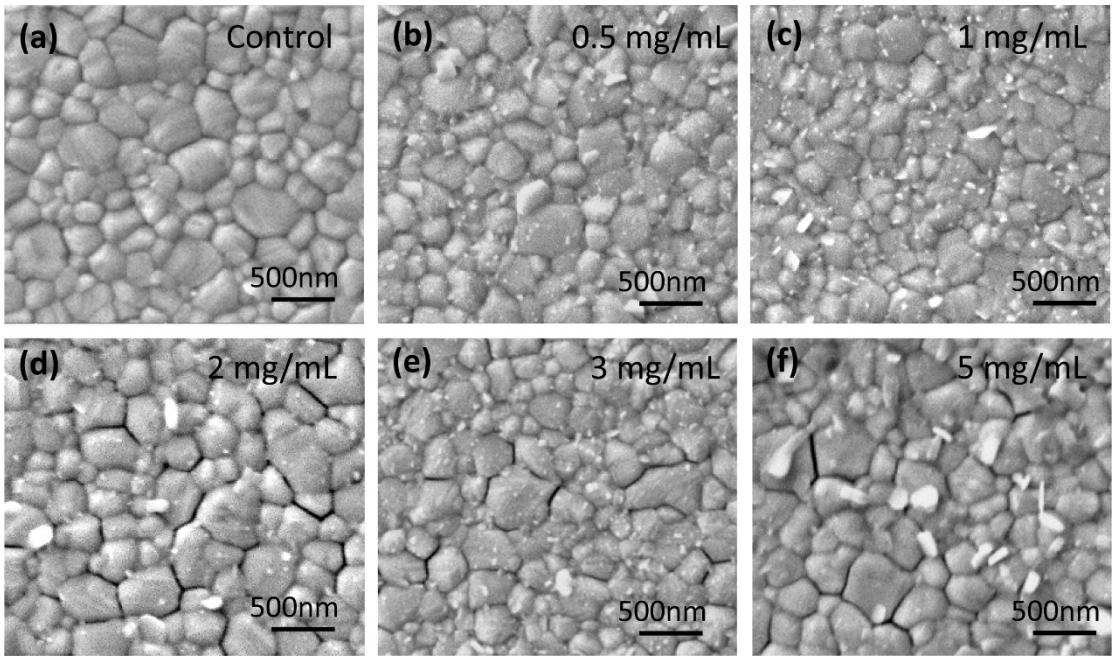

Figure 3. Surface SEM images of perovskite films with different AIBA concentrations. (a) 0 mg/mL (control), (b) 0.5 mg/mL, (c) 1 mg/mL, (d) 2 mg/mL, (e) 3 mg/mL and (f) 5 mg/mL.

The SEM image of the control perovskite film prepared by modified two-step is shown in Figure 3a. The perovskite film shows very uniform and condenses features

with full coverage upon PTAA substrates. Stone-shaped perovskite crystals are formed and large grain sizes up to ~500 nm are observed. When the AIBA concentration is below 1 mg/mL, the grain sizes of $MAPbI_3$ do not change that much, which indicates that this post-treatment method may not affect the crystallization of the perovskite grains (Figure 3b and Figure 3c). It is worth noticing that the GBs become blurred with AIBA introduction, which is similar to the effect of $MAPbI_3$ passivated by 4-dimethylaminobenzoic acid [11]. A thin layer composed of smaller particles is formed due to surface modification by AIBA. The GBs become more clear, and the obvious gaps are observed among the perovskite grains as the concentration of AIBA increases to 2 mg/mL, which indicates that high concentration AIBA cannot modify GBs (Figure 3d-3f). In addition, the physical gaps between grains may lead to decreased performance of the devices [51]. When the concentration of AIBA is 5 mg/mL, large AIBA particles appear (Figure 3f), which may be caused by the AIBA crystal agglomeration. Thus, the low concentration of AIBA (<2 mg/mL) may benefit the perovskite film performance. In order to confirm that the AIBA molecules can diffuse into GBs and improve the contact between grains, the SEM cross-sectional images of the devices without and with AIBA are collected, and the results are shown in Figures 4a, 4b and each layer is distinguished by a different color. It is noticed that the concentration of AIBA molecules is 1 mg/mL. From Figure 4a, the pristine perovskite film shows some clear GBs and large gaps between grains. Compared to the control device, the grains of the perovskite film with AIBA contact each other more closely, and the GBs are not easy to distinguish (Figure 4b). This is consistent with the top-view

SEM results. In addition, the interface between perovskite and cathode is also improved by AIBA introduction.

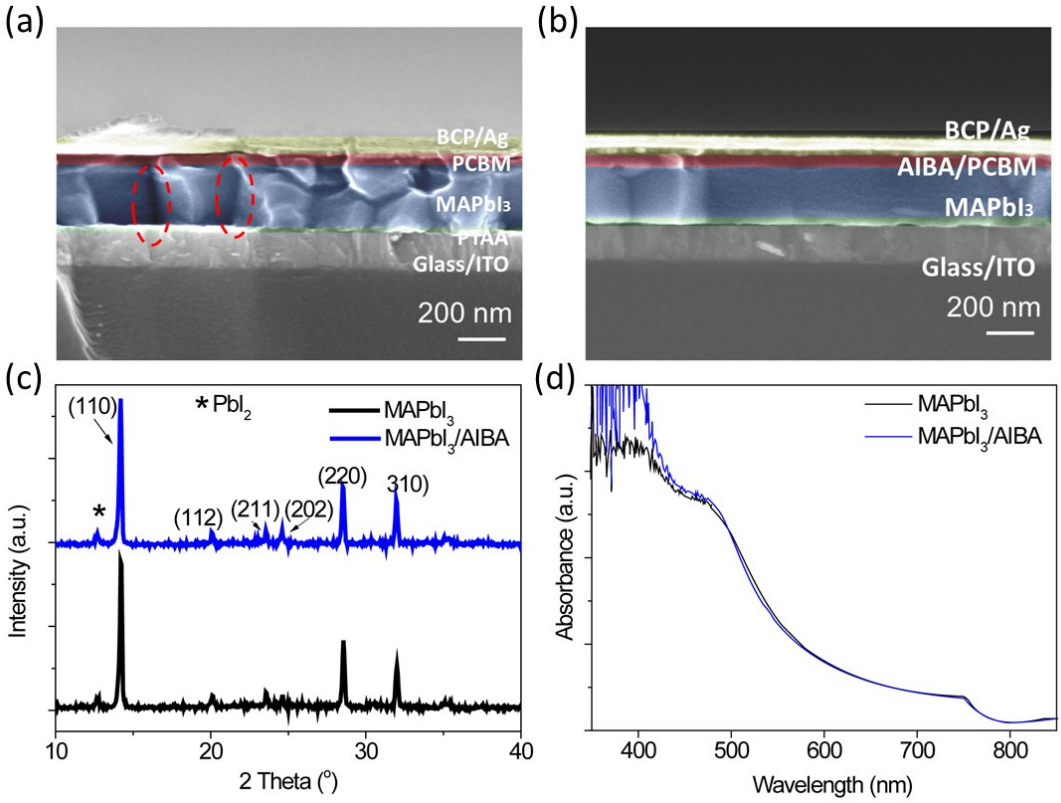

Figure 4. (a), (b) Cross-sectional SEM images of the devices without and with AIBA. (c) XRD diffraction patterns of the $MAPbI_3$ and $MAPbI_3$/AIBA films. (d) UV-vis absorption spectra of the $MAPbI_3$ and $MAPbI_3$/AIBA films.

To confirm the AIBA impact on the crystallinity of the $MAPbI_3$, XRD measurement is carried out and the results are shown in Figure 4c. Three main XRD peaks located at 14.20 °, 28.50 °, 31.95 ° are observed for the $MAPbI_3$ perovskite films with and without AIBA, and the intensity of the peaks are nearly the same. Thus, these two films exhibit similar crystallinity and identical crystal structure, which confirms

that AIBA doesn't impact the crystallinity of the $MAPbI_3$ films. The UV-vis absorption spectra of the two films are shown in Figure 4d and the absorbance of $MAPbI_3$/AIBA is similar to the $MAPbI_3$ film. However, the enhancement in the range of 350 nm - 490 nm is attributed to the intrinsic absorption of AIBA (Figure S1). The above statements confirm that the AIBA cannot impact the crystalline growth of the $MAPbI_3$ film and also doesn't change the $MAPbI_3$ crystal structure.

In order to investigate the influence of AIBA on the performance of the PSCs, the inverted devices with the structure shown in Figure 1a are fabricated. Firstly, the concentration of the AIBA is optimized. The photovoltaic parameters of PCE, fill factor (FF), short-circuit current density (J_{sc}), and open-circuit voltage (V_{oc}) at various AIBA concentrations are summarized in Figure 5a and Table 1. The typical J-V curves of the devices with different AIBA concentrations are shown in Figure 5b. The V_{oc}, FF, J_{sc} increase as the AIBA concentrations increase from 0.5 mg/mL to 1 mg/mL. The performance starts to degrade as the AIBA concentration further increases to 2 mg/mL and 3 mg/mL. The decreased performance is attributed to the deteriorated film morphology and increased grain gaps (Fig 3b-e) as the AIBA concentration is 1 mg/mL. The device with 1 mg/mL AIBA exhibits a high average PCE of 19.40 %, FF of 76.78 %, J_{sc} of 23.13 mA/cm^2, and V_{oc} of 1.09 V. The control devices show an average PCE of 18.92 %, FF of 76.74 %, J_{sc} of 22.96 mA/cm^{2,} and V_{oc} of 1.07 V. It is obvious that J_{sc}, FF and V_{oc} are enhanced by AIBA modification. It is worth to notice that the V_{oc} enhancement is more evident. The enhanced V_{oc} can be attributed to the elimination of the trap-assisted non-radiation recombination loss according to the literature [52, 53]. This

further confirms the surface trap states are reduced by AIBA introduction. The IPCE of the device with AIBA shows enhancement from 350 nm to 700 nm compared to the control device, which is consistent with the improved J_{sc}. The IPCE spectrum profile is different from other reported results [1, 54]. This is attributed to the transmittance of the ITO substrates. Figure S2 shows the transmission spectra of ITO substrates used in this work compared to other kind of ITO with different conductivity. The J-V curves of the optimized device with different scan directions are shown in Figure 5c. The high PCE of 20.23 %, with J_{sc} of 23.45 mA/cm^2, V_{oc} of 1.10 V, and FF of 78.07 % is achieved by the reverse scan with a scan speed of 80 mV/s. The device exhibits a PCE of 20.17 %, with J_{sc} of 23.40 mA/cm^2, V_{oc} of 1.10 V, and FF of 78.36 % for the forward scan direction. There is small PCE vibration with different scan directions. To quantitatively describe the hysteresis effect, equation 1 is used to calculate the HI [55].

$$\mathrm{HI} = \frac{PCE^{-} - PCE^{+}}{PCE^{-} + PCE^{+}} \quad (1)$$

The PCE^{-} is the PCE value derived from the reverse scan. The PCE^{+} is the PCE value derived from the forward scan. The calculated HI is 1.49 ‰. The trap states [56, 57] and ionic displacement/ion migration [58] are the main reasons for the hysteresis effect. Thus, the low HI is also correlated with the passivation function of AIBA. In addition, the stable PCE and J_{sc} values of the AIBA modified device measured at maximum power point are about ~20 % and ~21 mA/cm^2, respectively. The stable PCE and J_{sc} values of the control device measured at maximum power point are 18 % and 20 mA/cm^2, respectively. The improved stable PCE and J_{sc} of the modified device confirm the effects of the AIBA passivation on the PSC performance.

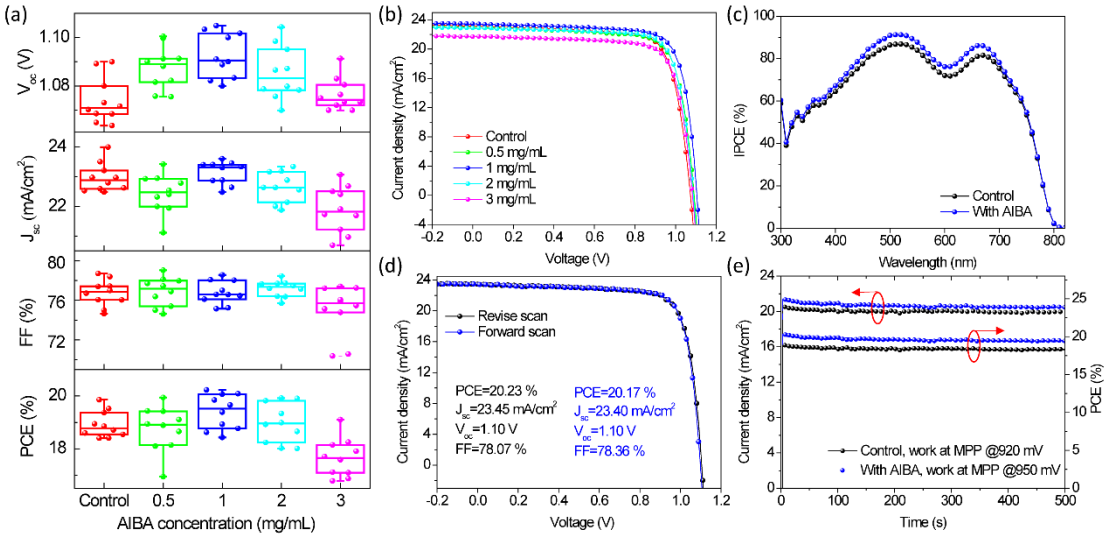

Figure 5. (a) Photovoltaic parameters (PCE, V_{oc}, FF, and J_{sc}) of PSCs with different AIBA concentrations derived from 10 devices. (b) The typical J-V curves of the devices with different AIBA concentrations. (c) The IPCE spectra of the PSCs with and without AIBA. (d) The J-V curves of the optimized device obtained with reverse and forward scan directions. (e) The steady-state output characteristic of the control and AIBA modified devices.

Table 1 The average photovoltaic parameters of the devices with various AIBA concentrations.

AIBA (mg/mL)	J_{sc} (mA/cm^2)	V_{oc} (V)	FF (%)	PCE (%)
0	22.96	1.07	76.74	18.92
0.5	22.43	1.09	76.86	18.76
1	23.13	1.09	76.78	19.40
2	22.64	1.09	77.18	18.98
3	21.88	1.08	75.02	17.66

To further understand the mechanisms of the improved device performance caused by AIBA introduction, EIS is used to investigate electrical dynamics in devices. The

Nyquist plots of the control and modified devices are shown in Figure 6a. Two semicircles can be fitted well with the equivalent circuit as shown in Figure S3 consisting of two parallel-RC elements and one series resistance (R_s). The fitting results are shown in Table S1. The lower frequency part is related to the recombination resistance (R_{rec}) and chemical capacitance (CPE1), while the high-frequency part is corresponding to the contact impedance (R_2 and CPE2) between perovskite and ETL or HTL. The PSC with AIBA shows a larger radius than the control device, and correspondingly shows a larger R_{rec} (7211 Ω) than that of the control device (4772 Ω). CPE1 values of the devices also reduce from 1.08×10^{-5} F to 6.15×10^{-6} F as AIBA is introduced to the devices, which may be related to the reduction of ions and carrier accumulation at electrode interface by AIBA [59]. AIBA introduction can reduce the non-radiation recombination loss and reduce the ion migration and trap states in devices, which is consistent with the improved V_{oc}. The TRPLwere measured under 460 nm light excitation and the result are shown in Figure S4. The PL decay curves are fitted by the bi-exponential function:

$$Y = A_1\, exp\left(\frac{-t}{\tau_1}\right) + A_2\, exp\left(\frac{-t}{\tau_2}\right) \quad (2)$$

The average decay time of the glass/$MAPbI_3$/AIBA is182.83 ns, which is longer than the pristine $MAPbI_3$ films (156.47 ns). The longer lifetime confirms that the non-radiative recombination is decreased and the carrier lifetime is enhanced via this AIBA surface treatment.

The Mott-Schottky analysis is also carried out to examine the built-in potential (V_{bi}) of the contact junction. Form Figure 6b and Figure 6c, the V_{bi} values of the AIBA

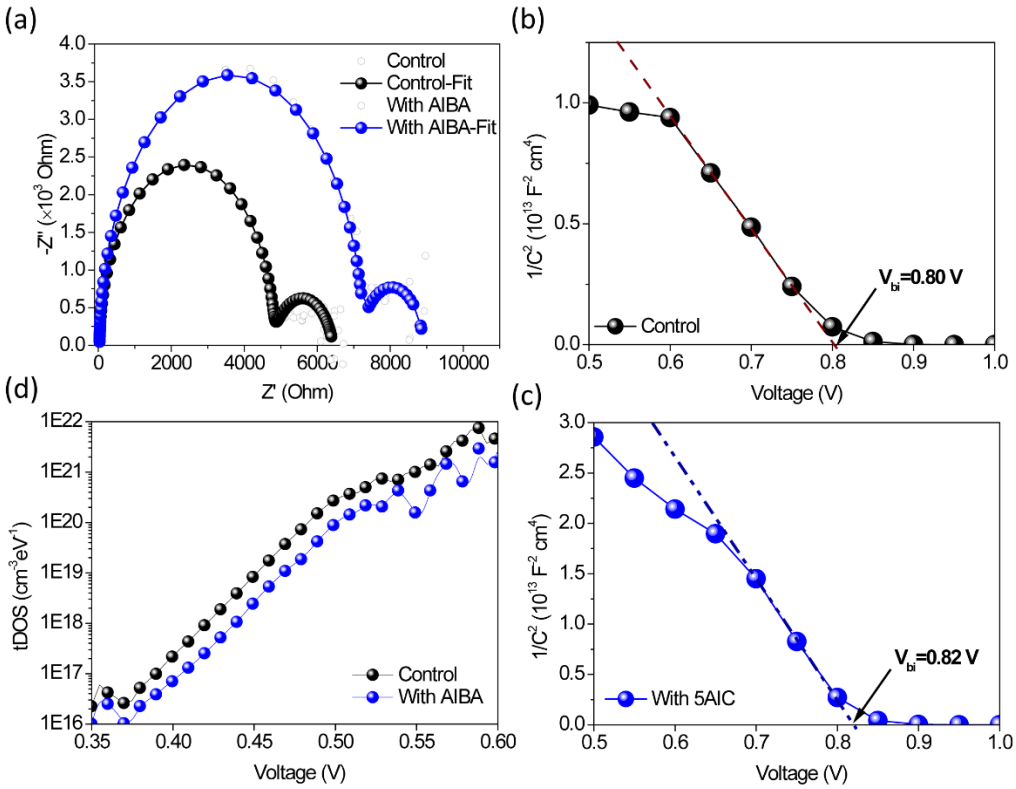

Figure 6. (a) Nyquist plots of PSCs with and without AIBA measured at a bias of 0.9 V under dark. (b), (c) Mott-Schottky curves for the control and AIBA PSCs. (d) The tDOS for the PSCs with and without AIBA.

device and control device are 0.82 V and 0.80 V, respectively. The enhanced V_{bi} could benefit the charge extraction and transport, which can avoid the charge accumulation at the interfaces between perovskite and charge transport layers and improve the performance of the devices [60]. In order to quantify the effect of AIBA on the defect passivation, the density of trap states with different energies can be calculated by the following equation based on the EIS data (Figure 6a) [42, 61], and the results are shown in Figure 6d.

$$C = -\frac{1}{\omega Z''} \tag{3}$$

$$N_t(E_\omega) = -\frac{V_{bi}}{eW}\frac{dC}{d\omega}\frac{\omega}{K_B T} \tag{4}$$

$$E_\omega = K_B T \, ln(\frac{\omega_0}{\omega}) \quad (5)$$

where C is the capacitance of the device; ω is the angular frequency; Z" is the imaginary part of the impendence; N_t is the trap density; W is the depletion layer width; K_B is the Boltzmann constant; T is the absolute temperature; ω_0 is the attempt-to-escape frequency ($\approx 10^{11}$ s^{-1}) [61], and E_ω is the energy demarcation. V_{bi} and W are extracted from the C-V results. From Figure 6d, the trap density-of-states (tDOS) with the energy level of 0.35 eV-0.60 eV for AIBA devices are lower than that of control, which indicates the shallow and deep trap states are efficiently suppressed [42, 61].

The AIBA can effectively passivate the defects at the surface and GBs of the perovskite films, which will impact the stability of the $MAPbI_3$ film as well as the corresponding devices. To test the UV light stability of the $MAPbI_3$ films, perovskite films are exposed to high power density UV light (365 nm @ 6 Watt). The UV light can combine with moisture, leading to serious device degradation [62]. Figure 7a is the photoluminescence (PL) spectra of the $MAPbI_3$ films vs UV irradiation time. The PL intensity of peak (763 nm) decreases rapidly under UV light irradiation. After AIBA introduction, the PL peak position doesn't change, and the peak intensity also decreases under this high power UV light irradiation (Figure 7b). The PL peak intensity influenced by the UV light irradiation time is shown in Figure 7c. The PL intensity of the modified film can maintain about 53.23 % of its initial value after 10 min UV light irradiation, while the control film can only maintain about 33.61 % of its initial value. After 50 min exposure to UV light, the PL intensity decay to 22.17 % and 13.71 % of their initial values for the $MAPbI_3$/AIBA and $MAPbI_3$, respectively. This result shows

the AIBA can enhance the UV light stability of the perovskite active layer, which may be related to the passivation effect and UV light absorption of AIBA (Figure S1). The moisture stability of the devices with and without AIBA is measured under different humidity environments, and the results are shown in Figure 7d and Figure 7e. The stability of the devices is derived from investigations of 12 devices prepared with the same experimental condition. At the low humidity (20-40 RH %), the average value PCE of control devices decays to 72.91 % of its initial value after 600 h. After the AIBA introduction, the modified devices can maintain ~83.41 % of their initial values. This indicates the moisture stability of the PSCs is enhance by AIBA. In order to furtherly demonstrate this enhancement effect of AIBA, the devices are exposed to a high humidity environment (55-70 RH %) controlled by an environmental chamber for 100 h. The AIBA devices also show improved stability than the control devices. The average PCE of the modified devices can maintain 64.06 % of its initial value, while that of the control devices keeps 45.59% of its initial value (Figure 7e). This improvement may result from the enhancement hydrophobicity of the film surface with AIBA coating (Figure S5). In addition to the moisture decay, the Ag-electrode-induced device structure degradation due to ion migration also results in serious decay of PCE in a short time [63]. The thermal stability of the PSCs in 36the air (20-40 RH %) is studied, and the results are shown in Figure 7f. In this experiment, the statistical data are derived from 8 devices. The average PCE value of control PSCs decreases to 49.46% of its initial value as the devices are kept at 85℃ for 300 min. Compared to the moisture

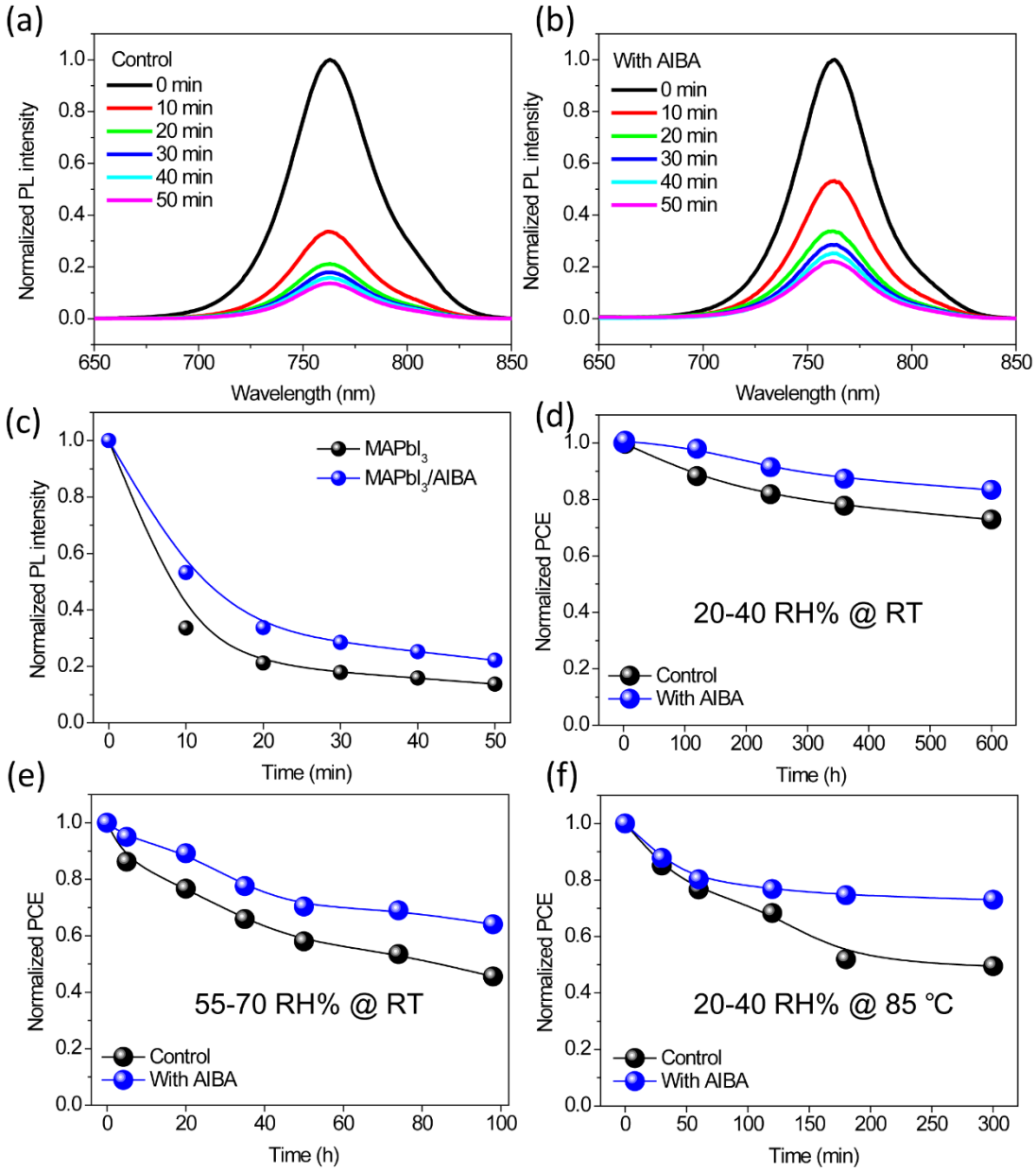

Figure 7. (a) The PL spectra of the $MAPbI_3$ film as a function of UV light irradiation time, (b) The PL spectra of the $MAPbI_3$/AIBA film as a function of UV light irradiation time, (c) The normalized PL intensity for $MAPbI_3$ and $MAPbI_3$/AIBA films. The stability of the devices under different condition: (d) 20-40 RH % at room temperature (RT), (e) 55-70 RH % at RT, (f) 20-40 RH % at 85℃.

stability under the same humidity at RT (Figure 7d), the thermal-induced degradation

is confirmed for the control device. This degradation is improved by AIBA. The PCE can maintain about 72.99 % of its initial value at 85℃ after 300 min. This improvement may be ascribed to two aspects. Firstly, the AIBA may suppress the ion migration by passivating GBs. Secondly, the AIBA can form an ion migration barrier layer between the perovskite and PCBM/BCP/Ag due to the perovskite film surface passivation.

CONCLUSION

In summary, we demonstrate novel, efficient and facile surface and GB passivation strategy by AIBA, which correspondingly improves the performance and stability of the PSCs. In addition, the calculation results show that the surface states induced by AIBA can facilitate the photoexcited charge transfer dynamics and reduce the electron-hole recombination loss. The highest PCE of 20.23 % and low hysteresis index (HI) of 1.49 ‰ are achieved in this study. Those numbers represent an excellent PCE and HI values for the inverted PSCs based on $MAPbI_3$/PCBM plana heterojunction. Moreover, the UV light stability of the perovskite films and the moisture stability of the devices are enhanced with the proposed passivation strategy. Furthermore, the thermal stability of the devices is also evidently improved due to the passivation and ion migration barrier function of AIBA. The passivation method developed in this work provides an efficient way to enhance the stability and performance of inverted PSCs. The combined experimental-computational study benefits the understanding of the surface passivation impact on the performance and stability of the inverted PSCs.

ASSOCIATED CONTENT

Supporting Information

The details of density functional theory (DFT) calculations is provided in the supporting information; The absorption spectra of AIBA; The equivalent circuit for EIS fitting; EIS parameters of the PSCs; The Supporting Information is available free of charge on the ACS Publications website at DOI:

AUTHOR INFORMATION

Corresponding Author

Email: qilin.dai@jsums.edu (QD)

Author contributions

J.X. conceived the experiments and wrote the original draft. P.N.S. performed the DFT study and wrote the calculation part. Y. Q., T. D., and K. W. characterized the performance of the films and materials. J. L. and Q.D. contributed to writing, review, and editing of the manuscript.

Fundings

This material is based on work supported by the National Science Foundation under Grant No. 1757220. The TRPL equipment used in this work is supported by National Science Foundation Research Initiation Award: Novel Perovskite Solar Cells Based on Interface Manipulation (Award#1900047).

Notes

The authors declare no competing financial interest.

ACKNOWLEDGMENT

This material is based on work supported by the National Science Foundation under Grant No. 1757220. The steady-state PL and TRPL equipment used in this work is supported by National Science Foundation Research Initiation Award: Novel Perovskite Solar Cells Based on Interface Manipulation (Award#1900047).

REFERENCES

(1) He, Z.; Xiong, J.; Dai, Q.; Yang, B.; Zhang, J.; Xiao, S., High-Performance Inverted Perovskite Solar Cells Using 4-Diaminomethylbenzoic as a Passivant. *Nanoscale* **2020,** *12*, 6767-6775

(2) NREL, Best Research-Cell Efficiencies, *https://www.nrel.gov/pv/cell-efficiency.html* (accessed: December, 2021).

(3) Zhu, P.; Gu, S.; Luo, X.; Gao, Y.; Li, S.; Zhu, J.; Tan, H., Simultaneous Contact and Grain-Boundary Passivation in Planar Perovskite Solar Cells Using SnO_2-KCl Composite Electron Transport Layer. *Adv. Energy Mater.* **2019,** *10* (3), 1903083.

(4) Li, Y.; Ji, L.; Liu, R.; Zhang, C.; Mak, C. H.; Zou, X.; Shen, H. H.; Leuf, S. Y.; Hsu, H. Y., A Review on Morphology Engineering for Highly Efficient and Stable Hybrid Perovskite Solar Cells. *J. Mater. Chem. A* **2018,** *6*, 12842-12875.

(5) Dunlap-Shohl, W. A.; Zhou, Y.; Padture, N. P.; Mitzi, D. B., Synthetic Approaches for Halide Perovskite Thin Films. *Chem. Rev.* **2019,** *119*, 3193-3295.

(6) Chen, H.; Wei, Q.; Saidaminov, M. I.; Wang, F.; Johnston, A.; Hou, Y.; Peng, Z.; Xu, K.; Zhou, W.; Liu, Z.; Qiao, L.; Wang, X.; Siwen Xu; Li, J.; Long, R.; Ke, Y.; Sargent, E. H.; Ning, Z., Efficient and Stable Inverted Perovskite Solar Cells Incorporating Secondary Amines. *Adv. Mater.* **2019,** *31* (46), 1903559.

(7) Kaltenbrunner, M.; Adam, G.; Głowacki, E. D.; Drack, M.; Schwödiauer, R.; Leonat, L.; Apaydin, D. H.; Groiss, H.; Scharber, M. C.; White, M. S.; Sariciftci, N.

S.; Bauer, S., Flexible High Power-Per-Weight Perovskite Solar Cells with Chromium Oxide-Metal Contacts for Improved Stability in Air. *Nat. Mater.* **2015,** *14* (10), 1032-1039.

(8) Meng, X.; Cai, Z.; Zhang, Y.; Hu, X.; Xing, Z.; Huang, Z.; Huang, Z.; Cui, Y.; Hu, T.; Su, M.; Liao, X.; Zhang, L.; Wang, F.; Song, Y.; Chen, Y., Bio-Inspired Vertebral Design for Scalable and Flexible Perovskite Solar Cells. *Nat. Common.* **2020,** *11*, 3016.

(9) Hu, X.; Huang, Z.; Zhou, X.; Li, P.; Wang, Y.; Huang, Z.; Su, M.; Ren, W.; Li, F.; Li, M.; Chen, Y.; Song, Y., Wearable Large-Scale Perovskite Solar-Power Source Via Nanocellular Scaffold. *Adv. Mater.* **2017,** *29* (42), 1703236.

(10) Zheng, X.; Hou, Y.; Bao, C.; Yin, J.; Yuan, F.; Huang, Z.; Song, K.; Liu, J.; Troughton, J.; Gasparini, N.; Zhou, C.; Lin, Y.; Xue, D.-J.; Chen, B.; Johnston, A. K.; Wei, N.; Mohamed Nejib Hedhili; Wei, M.; Alsalloum, A. Y.; Maity, P.; Turedi, B.; Yang, C.; Baran, D.; Anthopoulos, T. D.; Han, Y.; Lu, Z.-H.; Mohammed, O. F.; Gao, F.; Sargent, E. H.; Bakr, O. M., Managing Grains and Interfaces Via Ligand Anchoring Enables 22.3%-Efficiency Inverted Perovskite Solar Cells. *Nat. Energy* **2020,** *5*, 131-140.

(11) Zhu, H.; Huang, B.; Wu, S.; Xiong, Z.; Li, J.; Chen, W., Facile Surface Modification of $Ch_3nh_3pbi_3$ Films Leading to Simultaneously Improved Efficiency and Stability of Inverted Perovskite Solar Cells. *J. Mater. Chem. A* **2018,** *6*, 6255-6264.

(12) Xiao, Z.; Dong, Q.; Bi, C.; Shao, Y.; Yuan, Y.; Huang, J., Solvent Annealing of Perovskite-Induced Crystal Growth for Photovoltaic-Device Efficiency Enhancement. *Adv. Mater.* **2014,** *26*, 6503-6509.

(13) Chiang, C. H.; Nazeeruddin, M. K.; Gratzelc, M.; Wu, C. G., The Synergistic Effect of H_2o and Dmf Towards Stable and 20% Efficiency Inverted Perovskite Solar Cells. *Energy Environ. Sci.* **2017,** *10*, 808-817.

(14) Chen, W.; Wang, Y.; Pang, G.; Koh, C. W.; Djurišic, A. B.; Wu, Y.; Tu, B.; Liu, F.; Chen, R.; Woo, H. Y.; Guo, X.; He, Z., Conjugated Polymer-Assisted Grainboundary Passivation for Efficient Inverted Planar Perovskite Solar Cells. *Adv. Funct. Mater.* **2019,** *29* (27), 1808855.

(15) Lin, Y.; Shen, L.; Dai, J.; Deng, Y.; Wu, Y.; Bai, Y.; Zheng, X.; Wang, J.; Fang, Y.; Wei, H.; Ma, W.; Zeng, X. C.; Zhan, X.; Huang, J., π-Conjugated Lewis Base: Efficient Trap-Passivation and Charge-Extraction for Hybrid Perovskite Solar Cells. *Adv. Mater.* **2017,** *29* (7), 1604545.

(16) Bi, C.; Wang, Q.; Shao, Y.; Yuan, Y.; Xiao, Z.; Huang, J., Non-Wetting Surface-Driven High-Aspect-Ratio Crystalline Grain Growth for Efficient Hybrid Perovskite Solar Cells. *Nat. Common.* **2015,** *6*, 7747.

(17) Dai, Z.; Xiong, J.; Zhan, S.; Fan, B.; Zhao, Q.; Liu, W.; He, Z.; Yang, B.; Yang, J.; Xue, X.; Zhang, J., A Facile Air-Retreatment Strategy for Efficient Inverted Perovskite Solar Cells. *Phys. Status Solidi RRL* **2020,** *14* (6), 2000069.

(18) Lin, C. T.; Rossi, F. D.; Kim, J., Baker, J.; Ngiam, J.; Xu, B.; Pont, S.; Aristidou, N.; Haque, S. A.; Watson, T.; McLachlan, M. A.; Durrant, J. R., Evidence for Surface Defect Passivation as the Origin of the Remarkable Photostability of Unencapsulated Perovskite Solar Cells Employing Aminovaleric Acid as a Processing Additive. *J. Mater. Chem. A* **2019,** *7* (7), 3006-3011.

(19) Castro-Méndez, A. F.; Hidalgo, J.; Correa-Baena, J. P., The Role of Grain Boundaries in Perovskite Solar Cells. *Adv. Energy Mater.* **2019,** *9* (38), 1901489.

(20) Wu, B.; Nguyen, H. T.; Ku, Z.; Han, G.; Giovanni, D.; Mathews, N.; Fan, H. J.; Sum, T. C., Discerning the Surface and Bulk Recombination Kinetics of Organic–Inorganic Halide Perovskite Single Crystals. *Adv. Energy Mater.* **2016,** *6*, 1600551.

(21) Dualeh, A.; Tétreault, N.; Moehl, T.; Gao, P.; Nazeeruddin, M. K.; Grätzel, M., Effect of Annealing Temperature on Film Morphology of Organic–Inorganic Hybrid Pervoskite Solid-State Solar Cells. *Adv. Funct. Mater.* **2014,** *24* (21), 3250-3258.

(22) Yin, W.; Shi, T.; Yan, Y., Unusual Defect Physics in $Ch_3nh_3pbi_3$ Perovskite Solar Cell Absorber. *Appl. Phys. Lett.* **2014,** *104*, 063903.

(23) Braly, I. L.; deQuilettes, D. W.; Pazos-Outón, L. M.; Burke, S.; Ziffer, M. E.; Ginger, D. S.; Hillhouse, H. W., Hybrid Perovskite Films Approaching the Radiative Limit with over 90% Photoluminescence Quantum Efficiency. *Nat. Photonics* **2018,** *12*, 355-361.

(24) Hu, L.; Li, M.; Yang, K.; Xiong, Z.; Yang, B.; Wang, M.; Tang, X.; Zang,

Z.; Liu, X.; Li, B.; Xiao, Z.; Lu, S.; Gong, H.; Ouyang, J.; Sun, K., PEDT:PSS Monolayers to Enhance the Hole Extraction and Stability of Perovskite Solar Cells. *J. Mater. Chem. A* **2018,** *6*, 16583-16589.

(25) Guo, Y.; Ma, J.; Lei, H.; Yao, F.; Li, B.; Xiong, L.; Fang, G., Enhanced Performance of Perovskite Solar Cells Via Anti-Solvent Nonfullerene Lewis Base It-4f Induced Trap-Passivation. *J. Mater. Chem. A* **2018,** *6* (14), 5919-5925.

(26) Lee, J. W.; Bae, S. H.; Hsieh, Y. T.; Marco, N. D.; Wang, M.; Sun, P.; Yang, Y., A Bifunctional Lewis Base Additive for Microscopic Homogeneity in Perovskite Solar Cells. *Chem* **2017,** *3*, 290-302.

(27) Li, H.; Li, Y.; Li, Y.; Shi, J.; Zhang, H.; Xu, X.; Wu, J.; Wu, H.; Luo, Y.; Li, D.; Meng, Q., Synergistic Effect of Caprolactam as Lewis Base and Interface Engineering for Efficient and Stable Planar Perovskite Solar Cells. *Nano Energy* **2017,** *42*, 222-231.

(28) Fang, Z.; Chen, W.; Shi, Y.; Zhao, J.; Chu, S.; Zhang, J.; Xiao, Z., Dual Passivation of Perovskite Defects for Light-Emitting Diodes with External Quantum Efficiency Exceeding 20%. *Adv. Funct. Mater.* **2020,** *30* (12), 1909754.

(29) Yang, S.; Dai, J.; Yu, Z.; Shao, Y.; Zhou, Y.; Xiao, X.; Zeng, X. C.; Huang, J., Tailoring Passivation Molecular Structures for Extremely Small Open-Circuit Voltage Loss in Perovskite Solar Cells. *J. Am. Chem. Soc.* **2019,** *141*, 5781-5787.

(30) Alharbi, E. A.; Alyamani, A. Y.; Kubicki, D. J.; Uhl, A. R.; Walder, B. J.; Alanazi, A. Q.; Luo, J.; Burgos-Caminal, A.; Albadri, A.; Albrithen, H.; Alotaibi, M. H.; Moser, J.-E.; Zakeeruddin, S. M.; Giordano, F.; Emsley, L.; Grätzel, M., Atomic-Level Passivation Mechanism of Ammonium Salts Enabling Highly Efficient Perovskite Solar Cells. *Nat. Common.* **2019,** *10*, 3008.

(31) Wang, S.; Zhu, Y.; Liu, B.; Wang, C.; Ma, R., Introduction of Carbon Nanodots into Sno_2 Electron Transport Layer for Efficient and Uv Stable Planar Perovskite Solar Cells. *J. Mater. Chem. A* **2019,** *7* (10), 5353-5362.

(32) Zheng, X.; Chen, B.; Dai, J.; Fang, Y.; Bai, Y.; Lin, Y.; Wei, H.; Zeng, X. C.; Huang, J., Defect Passivation in Hybrid Perovskite Solar Cells Using Quaternary Ammonium Halide Anions and Cations. *Nat. Energy* **2017,** *2*, 17102.

(33) Gao, F.; Zhao, Y.; Zhang, X.; You, J., Recent Progresses on Defect Passivation toward Efficient Perovskite Solar Cells. *Adv. Energy Mater.* **2019,** *10* (13), 1902650.

(34) Mahapatra, A.; Prochowicz, D.; Tavakoli, M. M.; Trivedi, S.; Kumara, P.; Yadav, P., A Review of Aspects of Additive Engineering in Perovskite Solar Cells. *J. Mater. Chem. A* **2020,** *8* (1), 27-54.

(35) Wang, R.; Xue, J.; Wang, K.-L.; Wang, Z.; Luo, Y.; Fenning, D.; Xu, G.; Nuryyeva, S.; Huang, T.; Zhao, Y.; Yang, J. L.; Zhu, J.; Wang, M.; Tan, S.; Yavuz, I.; Houk, K. N.; Yang, Y., Constructive Molecular Configurations for Surface-Defect Passivation of Perovskite Photovoltaics. *Science* **2019,** *366* (6472), 1509-1513.

(36) Liu, C.; Yang, Y.; Rakstys, K.; Mahata, A.; Franckevicius, M.; Mosconi, E.; Skackauskaite, R.; Ding, B.; Brooks, K. G.; Usiobo, O. J.; Audinot, J. N.; Kanda, H.; Driukas, S.; Kavaliauskaite, G.; Gulbinas, V.; Dessimoz, M.; Getautis, V.; Angelis, F. D.; Ding, Y.; Dai, S.; Dyson, P. J.; Nazeeruddin, M. K., Tuning Structural Isomers of Phenylenediammonium to Afford Efficient and Stable Perovskite Solar Cells and Modules. *Nat. Common.* **2021,** *12*, 6394.

(37) Wang, F.; Geng, W.; Zhou, Y.; Fang, H. H.; Tong, C. J.; Loi, M. A.; Liu, L. M.; Zhao, N., Phenylalkylamine Passivation of Organolead Halide Perovskites Enabling High-Efficiency and Air-Stable Photovoltaic Cells. *Adv. Mater.* **2016,** *28* (45), 9986-9992.

(38) Wu, P.; Ma, X.; Zhao, B.; Liu, C.; Chen, Y.; Yang, G.; Li, X., Modifying Perovskite Solar Cells with L(+)-Cysteine at the Interface between Mesoporous Tio_2 and Perovskite. *Sustain. Energ. Fuels* **2020,** *4* (2), 878-883.

(39) Alanazi, A. Q.; Kubicki, D. J.; Prochowicz, D.; Alharbi, E. A.; Bouduban, M. E. F.; Jahanbakhshi, F.; Mladenovic, M.; Milic, J. V.; Giordano, F.; Ren, D.; Alyamani, A. Y.; Albrithen, H.; Albadri, A.; Alotaibi, M. H.; Moser, J.-E.; Zakeeruddin, S. M.; Rothlisberger, U.; Emsley, L.; Gratzel, M., Atomic-Level Microstructure of Efficient Formamidinium-Based Perovskite Solar Cells Stabilized by 5-Ammonium Valeric Acid Iodide Revealed by Multinuclear and Two-Dimensional Solid-State Nmr. *J. Am. Chem. Soc.* **2019,** *141* (44), 17659-17669.

(40) Tidhar, Y.; Edri, E.; Weissman, H.; Zohar, D.; Hodes, G.; Cahen, D.;

Rybtchinski, B.; Kirmayer, S., Crystallization of Methyl Ammonium Lead Halide Perovskites: Implications for Photovoltaic Applications. *J. Am. Chem. Soc.* **2014,** *136* (38), 13249-13256.

(41) Conings, B.; Baeten, L.; Dobbelaere, C. D.; D'Haen, J.; Manca, J.; Boyen, H. G., Perovskite-Based Hybrid Solar Cells Exceeding 10% Efficiency with High Reproducibility Using a Thin Film Sandwich Approach. *Adv. Mater.* **2014,** *26* (13), 2041-2046.

(42) Wang, Q.; Shao, Y.; Dong, Q.; Xiao, Z.; Yuan, Y.; Huang, J., Large Fill-Factor Bilayer Iodine Perovskite Solar Cells Fabricated by a Low-Temperature Solution-Process. *Energy Environ. Sci.* **2014,** *7*, 2359-2365.

(43) Li, W.; Lai, X.; Meng, F.; Li, G.; Wang, K.; Kyaw, A. K. K.; Sun, X. W., Efficient Defect-Passivation and Charge-Transfer with Interfacial Organophosphorus Ligand Modification for Enhanced Performance of Perovskite Solar Cells. *Sol. Energy Mater. Sol. Cells* **2020,** *211*, 110527.

(44) Fan, B.; He, Z.; Xiong, J.; Zhao, Q.; Dai, Z.; Zhang, Z.; Xue, X.; Yang, J.; Yang, B.; Zhang, J., Facile Precursor Stoichiometry Engineering for Efficient Inverted Perovskite Solar Cells without Any Dopants. *Org. Electron.* **2019,** *75*, 105396.

(45) Trivedi, M. K.; Branton, A.; Trivedi, D.; Shettigar, H.; Bairwa, K.; Jana, S., Fourier Transform Infrared and Ultraviolet-Visible Spectroscopic Characterization of Biofield Treated Salicylic Acid and Sparfloxacin. *Nat. Prod. Chem. Res.* **2015,** *3* (5), 1000186.

(46) Wu, S.; Zheng, G.; Lian, H.; Xing, J.; Shen, L., Chlorination and Oxidation of Aromatic Polyamides. I. Synthesis and Characterization of Some Aromatic Polyamides. *J. Appl. Polym. Sci.* **1996,** *61*, 415-420.

(47) Xiong, J.; Eedugurala, N.; Qi, Y.; Liu, W.; Benasco, A. R.; Zhang, Q.; Morgan, S. E.; Blanton, M. D.; Azoulay, J. D.; Dai, Q., Efficient and Stable Perovskite Solar Cells Via Shortwave Infrared Polymer Passivation. *Sol. Energy Mater. Sol. Cells* **2021,** *220*, 110862.

(48) Guo, P.; Ye, Q.; Yang, X.; Zhang, J.; Xu, F.; Shchukin, D.; Wei, B.; Wang, H., Surface & Grain Boundary Co-Passivation by Fluorocarbon Based Bifunctional

Molecules for Perovskite Solar Cells with Efficiency over 21%. *J. Mater. Chem. A* **2019,** *7* (6), 2497-2506.

(49) Chen, H. C.; Hung, C.-M.; Kuo, C. H., Synergistic Engineering of Natural Carnitine Molecules Allowing for Efficient and Stable Inverted Perovskite Solar Cells. *ACS Appl. Mater. Interfaces* **2021,** *13* (7), 8595–8605.

(50) Wang, K.; Liu, J.; Yin, J.; Aydin, E.; Harrison, G. T.; Liu, W.; Chen, S.; Mohammed, O. F.; Wolf, S. D., Defect Passivation in Perovskite Solar Cells by Cyano-Based Π-Conjugated Molecules for Improved Performance and Stability. *Adv. Funct. Mater.* **2020,** *30*, 2002861.

(51) Han, T. H.; Lee, J. W.; Choi, C.; Tan, S.; Lee, C.; Zhao, Y.; Dai, Z.; Marco, N. D.; Lee, S. J.; Bae, S. H.; Yuan, Y.; Lee, H. M.; Huang, Y.; Yang, Y., Perovskite-Polymer Composite Cross-Linker Approach for Highly-Stable and Efficient Perovskite Solar Cells. *Nat. Common.* **2019,** *10*, 520.

(52) Jiang, K.; Wu, F.; Zhang, G.; Chow, P. C. Y.; Ma, C.; Li, S.; Wong, K. S.; Zhu, L.; Yan, H., Inverted Planar Perovskite Solar Cells Based on CsI-Doped Pedot:Pss with Efficiency Beyond 20% and Small Energy Loss. *J. Mater. Chem. A* **2019,** *7*, 21662-21667.

(53) Wu, S.; Zhang, J.; Li, Z.; Liu, D.; Qin, M.; Cheung, S. H.; Lu, X.; Lei, D.; So, S. K.; Zhu, Z.; Jen, A. K.-Y., Modulation of Defects and Interfaces through Alkylammonium Interlayer for Efficient Inverted Perovskite Solar Cells. *Joule* **2020,** *4*, 1-15.

(54) Li, F.; Deng, X.; Qi, F.; Li, Z.; Liu, D.; Shen, D.; Qin, M.; Wu, S.; Lin, F.; Jang, S. H.; Zhang, J.; Lu, X.; Lei, D.; Lee, C. S.; Zhu, Z.; Jen, A. K. Y., Regulating Surface Termination for Efficient Inverted Perovskite Solar Cells with Greater Than 23% Efficiency. *J. Am. Chem. Soc.* **2020,** *142* (47), 20134-20142.

(55) Chen, H.; Li, K.; Liu, H.; Gao, Y.; Yuan, Y.; Yang, B.; Zhou, C., Dependence of Power Conversion Properties of Hole-Conductor-Free Mesoscopic Perovskite Solar Cells on the Loading of Perovskite Crystallites. *Org. Electron.* **2018,** *61*, 119-124.

(56) Shao, Y.; Xiao, Z.; Bi, C.; Yuan, Y.; Huang, J., Origin and Elimination of Photocurrent Hysteresis by Fullerene Passivation in $Ch_3nh_3pbi_3$ Planar Heterojunction

Solar Cells. *Nat. Commun.* **2014,** *5*, 5784.

(57) Jixian Xu, A. B., Alexander H. Ip, Wei Li, Oleksandr Voznyy, Riccardo Comin, Mingjian Yuan, Seokmin Jeon, Zhijun Ning, Jeffrey J. McDowell, Pongsakorn Kanjanaboos, Jon-Paul Sun, Xinzheng Lan, Li Na Quan, Dong Ha Kim, Ian G. Hill, Peter Maksymovych, Edward H. Sargen, Perovskite–Fullerene Hybrid Materials Suppress Hysteresis in Planar Diodes. *Nat. Common.* **2015,** *6*, 7081.

(58) Bastiani, M. D.; Dell'Erba, G.; Gandini, M.; D'Innocenzo, V.; Neutzner, S.; Kandada, A. R. S.; Grancini, G.; Binda, M.; Prato, M.; Ball, J. M.; Caironi, M.; Petrozza, A., Ion Migration and the Role of Preconditioning Cycles in the Stabilization of the J–V Characteristics of Inverted Hybrid Perovskite Solar Cells. *Adv. Energy Mater.* **2015,** *6* (2), 1501453.

(59) Hailegnaw, B.; Sariciftci, N. S.; Scharber, M. C., Impedance Spectroscopy of Perovskite Solar Cells: Studying the Dynamics of Charge Carriers before and after Continuous Operation. *Phys. Status Solidi A* **2020,** *217* (22), 2000291.

(60) Wang, T.; Cheng, Z.; Zhou, Y.; Liu, H.; Shen, W., Highly Efficient and Stable Perovskite Solar Cells Via Bilateral Passivation Layers. *J. Mater. Chem. A* **2019,** *7* (38), 21730.

(61) Tang, G.; You, P.; Tai, Q.; Wu, R.; Yan, F., Performance Enhancement of Perovskite Solar Cells Induced by Lead Acetate as an Additive. *Solar RRL* **2018,** *2* (6), 1800066.

(62) Niu, G.; Li, W.; Meng, F.; Wang, L.; Dong, H.; Qiu, Y., Study on the Stability of Ch3nh3pbi3 Films and the Effect of Post-Modification by Aluminum Oxide in All-Solid-State Hybrid Solar Cells. *J. Mater. Chem. A* **2014,** *2*, 705-710.

(63) Jiangwei Li, Q. D., Nan Li, Liduo Wang, Direct Evidence of Ion Diffusion for the Silver-Electrode-Induced Thermal Degradation of Inverted Perovskite Solar Cells. *Adv. Energy Mater.* **2017,** *7* (14), 602922.

For Table of Contents Only

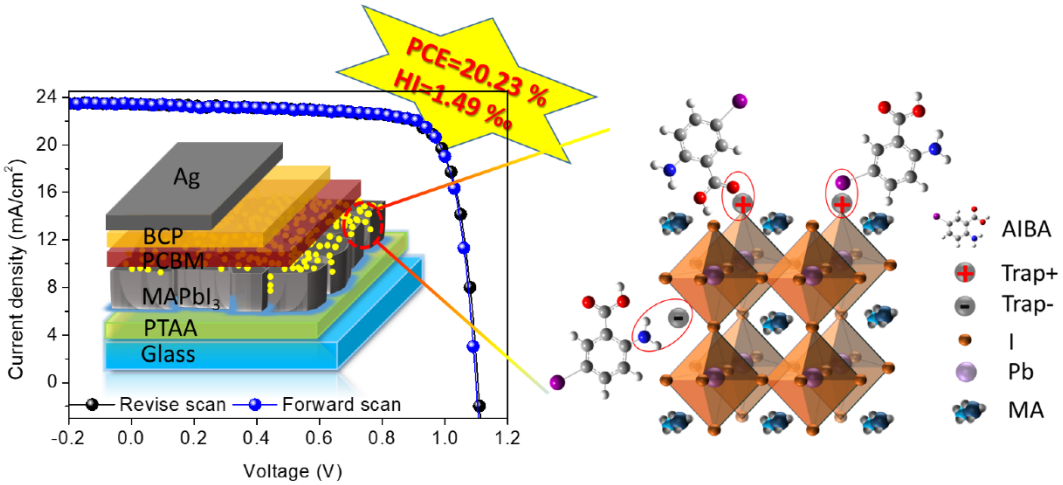

Supporting Information

Enhanced perovskite solar cell performance via 2-amino-5-iodobenzoic acid passivation

*Jian Xiong, Pabitra Narayan Samanta, Yifang Qi, Teresa Demeritte, Kira Williams, Jerzy Leszczynski, and Qilin Dai**

Department of Chemistry, Physics and Atmospheric Sciences, Jackson State University, Jackson, MS, 39217, USA

* Corresponding author: Q. Dai, Email: qilin.dai@jsums.edu

Computational Details

To estimate the formation energies of neutral and charged point defects, all the model structures of the PbI_2-rich $MAPbI_3$ (001) surface are fully relaxed within the framework of spin-polarized density functional theory (DFT) by employing Monkhorst-Pack sampling with a 4 × 4 × 1 k-point grid and a mesh cut-off energy of 185 Hartree. The slab models are constructed by retaining a vacuum space of more than 15 Å in the Z-direction in tandem with the dipole correction to annihilate the fictitious interaction with its periodic images. The electronic energies of each slab model are computed by adopting generalized gradient approximation (GGA)-based Perdew–Burke–Ernzerhof (PBE) [1] exchange-correlation functional and double zeta polarized (DZP) basis sets together with the SG15 Optimized Norm-Conserving Vanderbilt (ONCV) pseudopotentials [2] for all the constituent atoms. All of the atomic positions are relaxed until the residual forces on each atom are less than 0.05 eV/Å. Next, to examine the impact of relativistic effects on the electronic ground state of the perovskite material due to the presence of heavy elements (Pb and I), the electronic energies of the

PbI_2-rich $MAPbI_3$ surface with and without elementary vacancy defect are derived by performing spin-orbit (SO) DFT calculations. However, the relative stability of the pristine surface and surfaces with elemental intrinsic defects is retained as predicted by the PBE DFT method without spin-orbit correction. Furthermore, the spin-polarized DFT computation without SO interaction is found to be an efficient approach in reproducing the experimental optical gap as evident by the simulated optical spectra. The formation energy of native point defects in $MAPbI_3$ terminated with PbI_2 is then evaluated as follows:

$$E_f(X^q) = E_{tot}(X^q) - E_{tot}(surface) - E_X$$

where $E_{tot}(X^q)$ refers to the total energy of the perovskite supercell comprising the elementary vacancy defect X with charge q; $E_{tot}(surface)$ denotes the total energy of the pristine surface; and E_X is the chemical potential of the corresponding ion. Similarly, to assay the nature of binding of passivating molecule AIBA with the PbI_2-rich $MAPbI_3$ surface containing charge defects, the total energies of the passivated surfaces ($MAPbI_3$/AIBA) with and without vacancy defect are further calculated at the spin-polarized PBE/DZP level of theory. All DFT computations were performed using the QuantumWise ATK software package [3].

References

[1] Perdew, J. P.; Burke, K.; Ernzerhof, M. Generalized Gradient Approximation Made Simple. *Phys. Rev. Lett.* **1996**, 77, 3865.

[2] Hamann, D. R. Optimized norm-conserving Vanderbilt pseudopotentials. *Phys. Rev. B* **2013**, 88, 085117.

[3] Atomistix ToolKit version 2017.2, QuantumWise A/S (www.quantumwise.com).

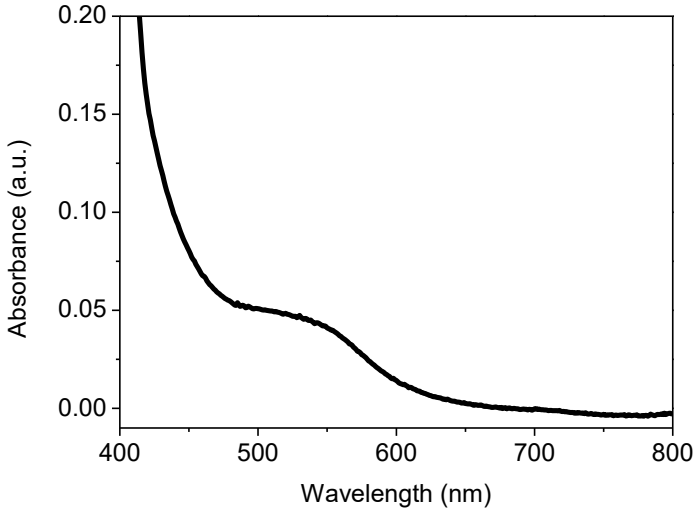

Figure S1. The absorption spectra of AIBA.

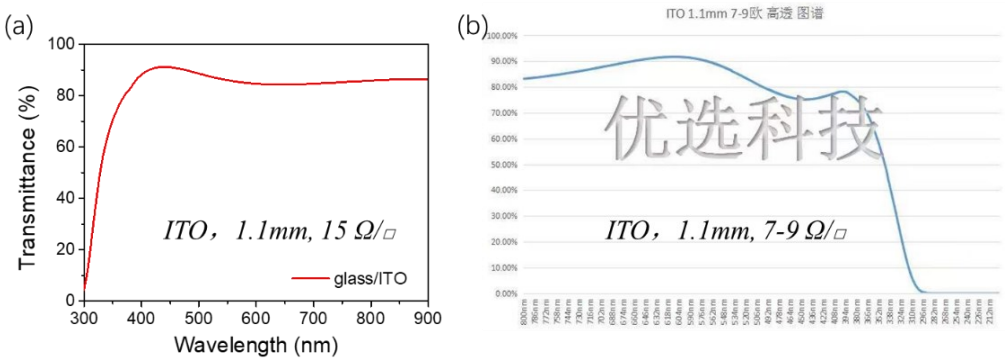

Figure S2. The transmittance of the ITO substrates with 15 Ω/□ (left) and 7-9 Ω/□ used in this work (right).

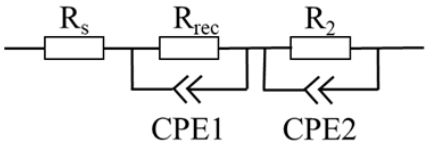

Figure S3. The equivalent circuit for EIS fitting.

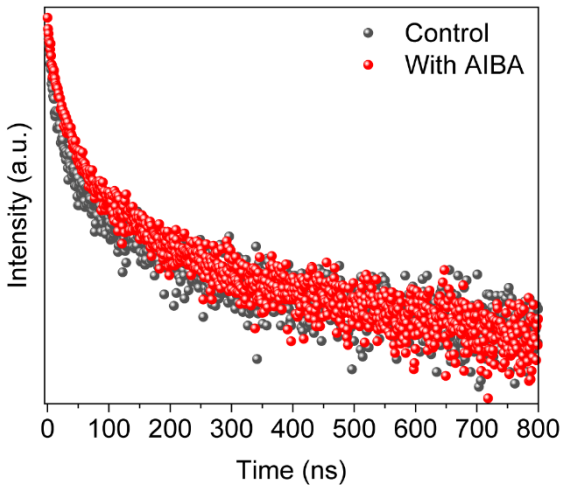

Figure S4. The The TRPL spectra of the glass/$MAPbI_3$, glass/$MAPbI_3$/AIBA. The PL decay curves are fitted by bi-exponential function ($Y = A_1\, exp\left(\frac{-t}{\tau_1}\right) + A_2\, exp\left(\frac{-t}{\tau_2}\right)$) and the average decay time of the pristine $MAPbI_3$ films, glass/$MAPbI_3$/AIBA are 156.47 ns and 182.83 ns, respectively.

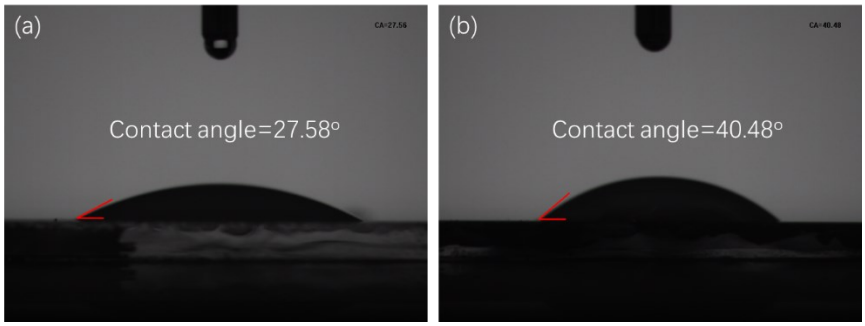

Figure S5. The water contact angle of $MAPbI_3$ and $MAPbI_3$/AIBA.

Table S1. EIS parameters of the PSCs.

Sample	R_s (Ω)	R_{rec} (Ω)	R_2 (Ω)	CPE1 (F)	CPE2 (F)
Control	35.57	4772	1623	1.08×10^{-5}	3.43×10^{-8}
With AIBA	35.22	7211	1659	6.15×10^{-6}	3.49×10^{-9}

Supporting Information

Enhanced perovskite solar cell performance via 2-amino-5-iodobenzoic acid passivation

*Jian Xiong, Pabitra Narayan Samanta, Yifang Qi, Teresa Demeritte, Kira Williams, Jerzy Leszczynski, and Qilin Dai**

Department of Chemistry, Physics and Atmospheric Sciences, Jackson State University, Jackson, MS, 39217, USA

* Corresponding author: Q. Dai, Email: qilin.dai@jsums.edu

Computational Details

To estimate the formation energies of neutral and charged point defects, all the model structures of the PbI_2-rich $MAPbI_3$ (001) surface are fully relaxed within the framework of spin-polarized density functional theory (DFT) by employing Monkhorst-Pack sampling with a 4 × 4 × 1 k-point grid and a mesh cut-off energy of 185 Hartree. The slab models are constructed by retaining a vacuum space of more than 15 Å in the Z-direction in tandem with the dipole correction to annihilate the fictitious interaction with its periodic images. The electronic energies of each slab model are computed by adopting generalized gradient approximation (GGA)-based Perdew–Burke–Ernzerhof (PBE) [1] exchange-correlation functional and double zeta polarized (DZP) basis sets together with the SG15 Optimized Norm-Conserving Vanderbilt (ONCV) pseudopotentials [2] for all the constituent atoms. All of the atomic positions are relaxed until the residual forces on each atom are less than 0.05 eV/Å. Next, to examine the impact of relativistic effects on the electronic ground state of the perovskite material due to the presence of heavy elements (Pb and I), the electronic energies of the

PbI_2-rich $MAPbI_3$ surface with and without elementary vacancy defect are derived by performing spin-orbit (SO) DFT calculations. However, the relative stability of the pristine surface and surfaces with elemental intrinsic defects is retained as predicted by the PBE DFT method without spin-orbit correction. Furthermore, the spin-polarized DFT computation without SO interaction is found to be an efficient approach in reproducing the experimental optical gap as evident by the simulated optical spectra. The formation energy of native point defects in $MAPbI_3$ terminated with PbI_2 is then evaluated as follows:

$$E_f(X^q) = E_{tot}(X^q) - E_{tot}(surface) - E_X$$

where $E_{tot}(X^q)$ refers to the total energy of the perovskite supercell comprising the elementary vacancy defect X with charge q; $E_{tot}(surface)$ denotes the total energy of the pristine surface; and E_X is the chemical potential of the corresponding ion. Similarly, to assay the nature of binding of passivating molecule AIBA with the PbI_2-rich $MAPbI_3$ surface containing charge defects, the total energies of the passivated surfaces ($MAPbI_3$/AIBA) with and without vacancy defect are further calculated at the spin-polarized PBE/DZP level of theory. All DFT computations were performed using the QuantumWise ATK software package [3].

References

[1] Perdew, J. P.; Burke, K.; Ernzerhof, M. Generalized Gradient Approximation Made Simple. *Phys. Rev. Lett.* **1996**, 77, 3865.

[2] Hamann, D. R. Optimized norm-conserving Vanderbilt pseudopotentials. *Phys. Rev. B* **2013**, 88, 085117.

[3] Atomistix ToolKit version 2017.2, QuantumWise A/S (www.quantumwise.com).

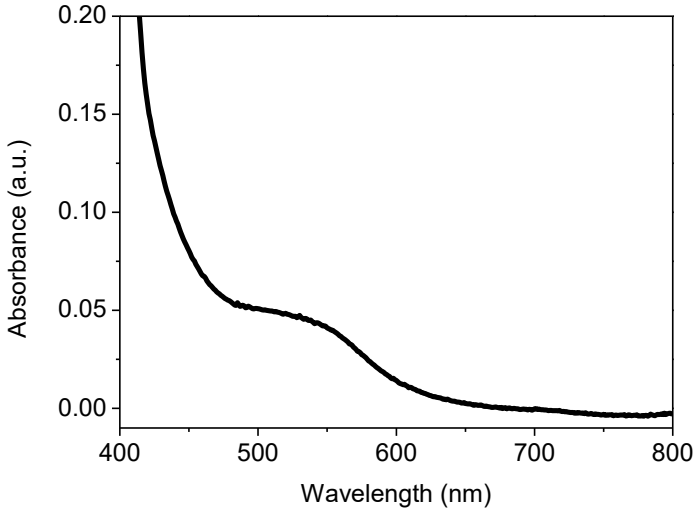

Figure S1. The absorption spectra of AIBA.

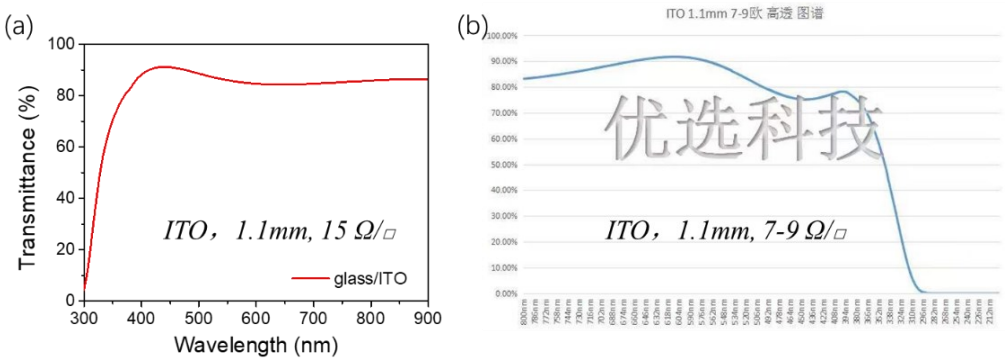

Figure S2. The transmittance of the ITO substrates with 15 Ω/□ (left) and 7-9 Ω/□ used in this work (right).

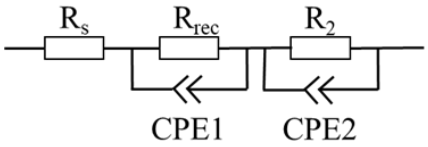

Figure S3. The equivalent circuit for EIS fitting.

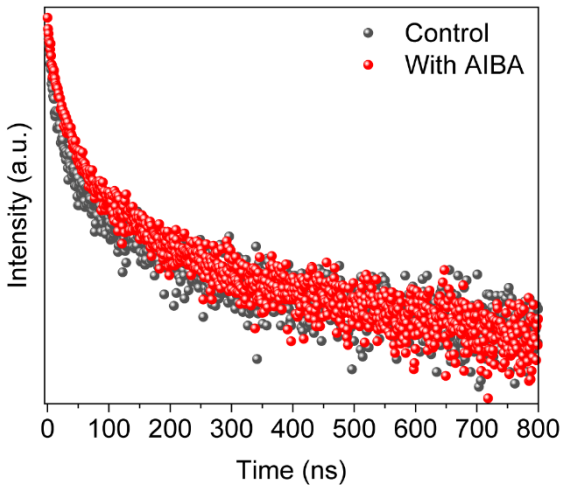

Figure S4. The The TRPL spectra of the glass/$MAPbI_3$, glass/$MAPbI_3$/AIBA. The PL decay curves are fitted by bi-exponential function ($Y = A_1\, exp\left(\frac{-t}{\tau_1}\right) + A_2\, exp\left(\frac{-t}{\tau_2}\right)$) and the average decay time of the pristine $MAPbI_3$ films, glass/$MAPbI_3$/AIBA are 156.47 ns and 182.83 ns, respectively.

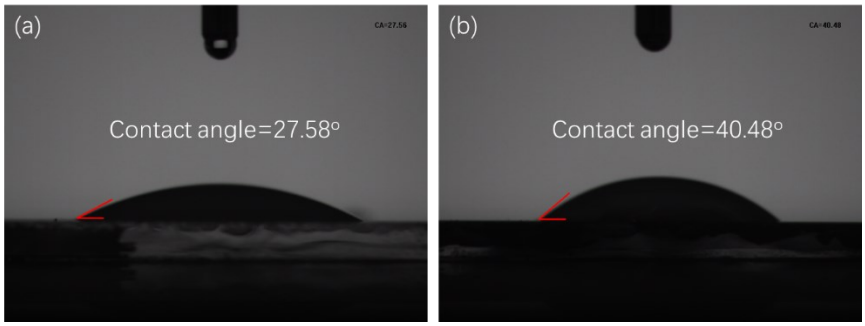

Figure S5. The water contact angle of $MAPbI_3$ and $MAPbI_3$/AIBA.

Table S1. EIS parameters of the PSCs.

Sample	R_s (Ω)	R_{rec} (Ω)	R_2 (Ω)	CPE1 (F)	CPE2 (F)
Control	35.57	4772	1623	1.08×10^{-5}	3.43×10^{-8}
With AIBA	35.22	7211	1659	6.15×10^{-6}	3.49×10^{-9}